Contactless thermal profilometry of carbon-resin materials by IR thermography

Marie-Marthe Groz, Alain Sommier, Emmanuelle Abisset-Chavanne, Stéphane Chevalier, Anissa Meziane, Jean-Christophe Batsale, Christophe Pradere

Contactless thermal profilometry of carbon-resin materials by IR thermography

Marie-Marthe Groz[a, 1], Alain Sommier[a], Emmanuelle Abisset-Chavanne[a], Stephane Chevalier[a], Anissa Meziane[a], Jean-Christophe Batsale[a] and Christophe Pradere[a]

[a] I2M CNRS-UB-ENSAM, Esplanade des arts et métiers, 33405 Talence Cedex, France.
[1] Correspondence: marie-marthe.groz@u-bordeaux.fr

Abstract

In this paper, we addressed the problem of quantitatively measuring the profile of bilayer media. A contactless thermal profilometry method is proposed. Concretely, this approach corresponds to measuring the interface between two media of a material. An experimental setup is proposed, and a methodology is presented to estimate the profile . Two examples, one numerical and one experimental, are presented in order to validate the method.

1 Introduction

A profilometer is an instrument that is used to measure the surface condition, the relief of a surface, in order to evaluate its roughness or microgeometry. The two main devices currently used for profilometry are contact profilometers, based on the physical contact between a diamond tip and the surface to be measured [1], and contactless optical profilometers [2] that allow measuring the distance between the sensor and the surface being studied. The optical coherence tomography technique (OCT), for example, use the echo principle [3] and is widely employed in bio-medical domain and art conservation [4]. It is a very useful technique for sub-surface imaging but is limited in depth. The principle of the opto-acoustic imaging is another contactless optical technique. It is based on the photoacoustic effect. A non-ionizing laser pulse is delivered and in some media, a part of the laser energy is absorbed and converted into heat, leading to transient thermoelastic expansion and thus wideband ultrasonic emission [5, 6]. This method is particularly well-suited for bio-medical media, because in the biological tissues the thermoelastic expansion is high enough to generate a measurable ultrasonic emission [7]. In this paper, a contactless thermal profilometer is proposed to be complementary to these techniques. The principle is schematized by figure 1.

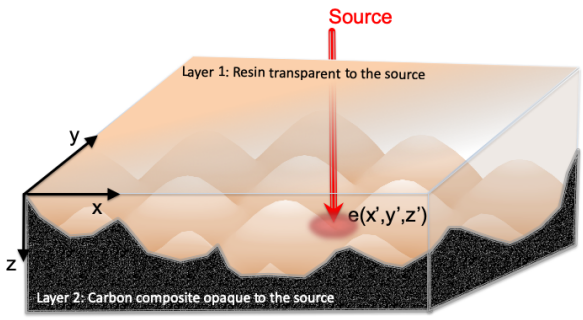

Fig. 1: Scheme of the contactless thermal profilometry principle

Concretely, this approach corresponds to measuring the interface between two media of a material. As already used in the pioneering work of Burgholzer *et al.* [8, 9, 10] and Mendioroz *et al.* [11, 12, 13, 14, 15] for source shape reconstruction and super-resolution approaches, the principle of the method presented here is to create a buried point such as a heat source that becomes a source of energy in the material. From this heat generation, 3D transient thermal diffusion will occur into the sample, and the resulting surface temperature may be monitored using an IR camera. From these transient temperature fields, an inverse processing method based on the model presented by Groz *et al.* [16, 17] is used. The complete 3D transient model can be adapted in order to find the position of the source and therefore the thickness between this point source and the surface of the material. The complete profile of the buried interface can then be measured with the flying spot setup proposed by [18] and depicted in figure 2. This method enables simply repeating the overall process to elucidate the complete sample surface

by laser scanning.

Contrary to the previous work of Burgholzer *et al.* and Mendioroz *et al.*, the objective here is not to reconstruct the source or the shape of the buried sources but to estimate the exact depth of the source in order to perform contactless profilometry. Moreover, the idea is to use the separability of the impulse response [19] and to use the 1D transient problem (relative to the maximum 3D temperature field) as already depicted in the work of Holland [20].

2 Experimental setup

The utilized experimental setup illustrated in figure 2 was originally developed for in-plane thermal diffusivities mapping by Gaverina *et al.* [18]. This consists of a laser diode (wavelength 976 nm) with 330 mW theoretical maximum power.

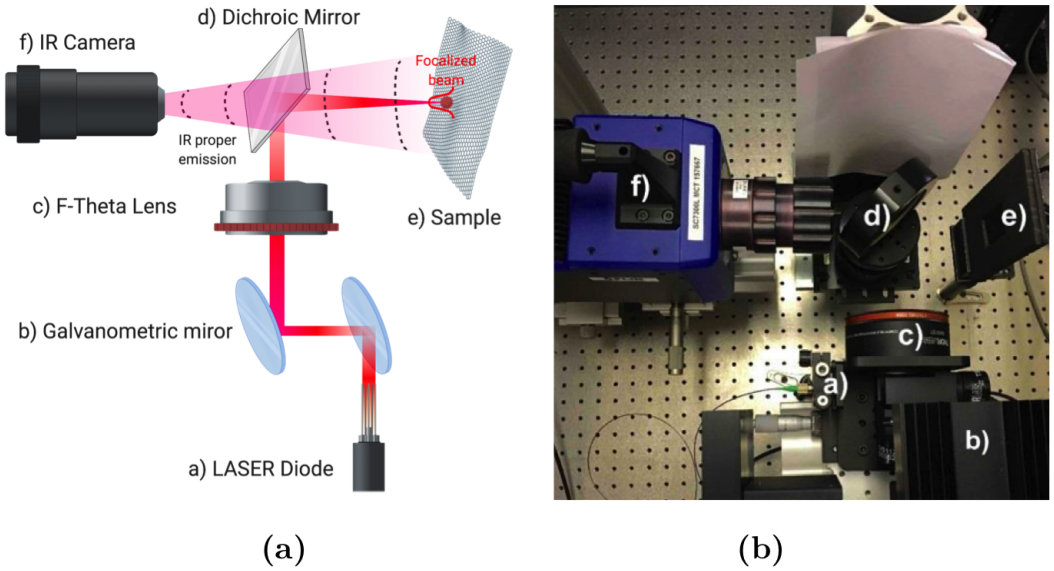

(a) (b)

Fig. 2: a) Schematic representation of the flying spot experimental setup and b) photograph of the bench.

To collimate the laser beam, an optical collimator system (Thorlabs) was used. A dual-axis scanning galvanometric system (Thorlabs GVS112/M) was used to control the spatial displacement of the laser spot. The principle of the laser beam deviation towards the sample is shown in figure 2. To focus the laser beam on the surface, an f-theta scan lens was used with a focusing length of 160 mm. With this focal length, the scanning area is equal to a square of 11 cm by 11 cm, and the resulting diameter of the focused spot is 26 μm, with a minimum displacement of 4.5 μm. In practice, the angular positions of the galvanometric system are related to a couple of coordinates expressed as voltage (V). This laser diode is mounted horizontally, and the beam is

reflected with a dichroic mirror (MD, treated to reflect 95% of the visible light from 700 nm to 1000 nm and to transmit 95% of the infrared radiation between 2 and 16 μm). To measure the temperature fields, an MCT IR camera (FLIR SC7000, 320 by 256 pixels, pitch 30 μm, spectral band from 9 to 11 μm) was used with an infrared objective lens (focal length 25 mm). Finally, the resulting spatial resolution with this setup can be between 100 to 300 μm approximately [21]. In this paper, the spatial resolution was 320 μm.

The exposed surface of the studied sample can be of any geometry, but this topography must be known to compute the proposed method. Indeed, in each area of measure, the IR-Camera must be parallel to the studied surface, but the positioning of the sample in order to achieve it for each measure can be made automatically with the help of a robot [21].

In a bilayer, as illustrated by figure 1, the only real constraint is to have a laser with a wavelength that is semitransparent to the surface material layer of the sample (layer 1 in figure 1). On the other hand, the buried layer for which the profile will be measured must effectively absorb the incident source wavelength. One of the advantages of this technique is that it can work in media that are opaque to visible. In industrial fields, this system can be generalized in a wide range of applications. For example, in aeronautical domain, some composite are coated with a resin. Some materials, like the silicium, vastly used in electronic devices, are opaque to visible, but can be semi-transparent in the IR.

Different types of laser scanning can be used, as illustrated in figure 3. These examples are important because, as will be analyzed in section 3.2.1, one configuration could be better than another depending on the need.

a) **b)** **c)**

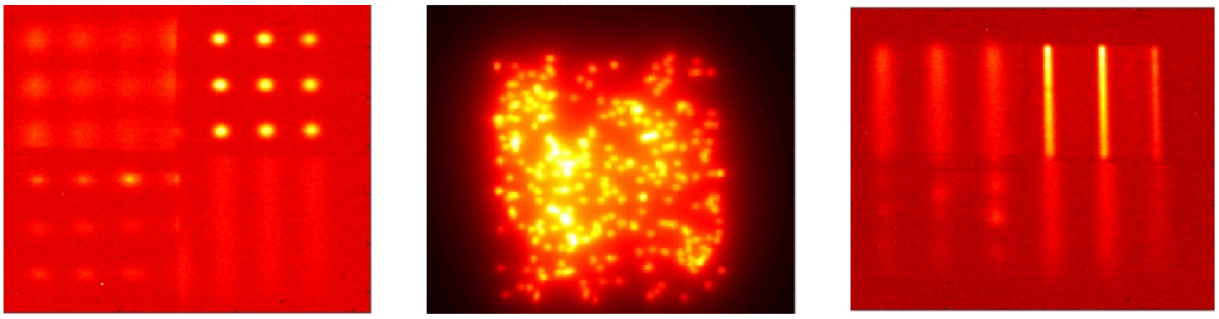

Fig. 3: Example of the temperature field measured after different types of laser scanning: a) pulsed grid, b) random and c) constant velocity.

Finally, an important point is the ability of the system to be calibrated in space and time. Indeed, during the different scans shown in figure 3, the positions and times relative to each laser pulse

are recorded in a file that will be used in postprocessing. This crucial step allows for a perfect spatial and temporal localization of the laser sources.

3 Description of the profilometry method

3.1 Presentation of the method for a unique point source

The proposed inverse method is based on the method of source reconstruction proposed in [17], which is based on the following 3D impulse thermal response at each point $r = (x, y, z)$ at time t from a heat source located at $r' = (x', y', z')$ delivering a pulse of heat quantity Q (J) at time $t = t_0$ in an orthotropic homogeneous medium:

$$\theta_{\text{Dirac}}(x, y, z, t) = \frac{Q(x', y', z')}{\rho C_p} \frac{\exp\left(-\frac{(x-x')^2}{4a_x(t-t_0)}\right)}{\sqrt{4\pi a_x(t-t_0)}} \frac{\exp\left(-\frac{(y-y')^2}{4a_y(t-t_0)}\right)}{\sqrt{4\pi a_y(t-t_0)}} \frac{\exp\left(-\frac{(z-z')^2}{4a_z(t-t_0)}\right)}{\sqrt{4\pi a_z(t-t_0)}} \quad (1)$$

where a_x, a_y and a_z ($\text{m}^2{\cdot}\text{s}^{-1}$) are the diffusivities along each of the x, y or z directions of space, respectively. ρ ($\text{kg}{\cdot}\text{m}^{-3}$) is the density and C_p ($\text{J}{\cdot}\text{K}^{-1}{\cdot}\text{kg}^{-1}$) the specific heat of the material.

The method of source reconstruction presented does not involve any prior information on the sources, and in particular, it enables finding several sources in depth. However, in the case of thermal profilometry, it is known that there is only one source in depth due to the laser absorption at the interface between the semitransparent resin layer and the opaque composite layer. Thus, the goal is only to estimate the position of the source along the z-axis. With this assumption, the whole model of equation 1 can be simplified according to the schema of figure 1 to obtain the surface temperature resulting from the heat source located at (x', y', z').

The laser impact, shown in figure 3 and schematized in figure 1, creates a heat point source pulsed at the interface between the laser-transparent layer and the absorbent layer. If there is only one impact on the sample, at the point (x', y', z'), the temperature at any point on the material is then given by equation 1. Since there is only one source point to be determined, the vectorial temperature (or thermogram) at the surface of the impact occurring at (x', y', z') is given by:

$$\theta_{x'y'0}(t) = \theta_{\text{Dirac}}(x = x', y = y', z = 0, t) = \frac{Q}{8\rho C_p} \frac{\exp\left(-\frac{z'^2}{4a_z(t-t_0)}\right)}{\sqrt{a_x a_y a_z(\pi(t-t_0))^3}} \quad (2)$$

It is noted that equation 2 is very close to the 1D impulse thermal response from a point source. The main difference arises from the diffusions along the x and y directions that are taken into account, which comes from the fact that the model chosen is 3D. Equation 2 can then be written as:

$$-\log\left(\sqrt{a_x a_y a_z(\pi(t-t_0))^3}\theta_{x'y'0}(t)\right) = \frac{z'^2}{4a_z(t-t_0)} - \log\left(\frac{Q}{8\rho C_p}\right) \tag{3}$$

By writing the following variable changes $Y(t-t_0) = -\log\left(\sqrt{a_x a_y a_z(\pi(t-t_0))^3}\theta_{x'y'0}(t)\right)$ and $X(t-t_0) = 1/(t-t_0)$, equation 3 becomes a linear formulation, depicted by equation 4.

$$Y(t-t_0) = \frac{z'^2}{4a_z}X(t-t_0) - \log\left(\frac{Q}{8\rho C_p}\right) \tag{4}$$

By the knowledge of the thermal diffusivity along the z-direction and from the slope estimation, the depth z' can be determined. This depth corresponds to the profile of the studied interface. It is important to note that this proposed method requires the knowledge of the diffusivity of the studied layer. If this parameter is not given, it can be determined by front- or rear-face flash methods for istropic materials [22] and logarithmical parabolic method for orthotropic ones [18].

It is noted that instead of just taking the temperature above the impact, one can also average (in space) the temperature at the surface of the material; equation 2 would then be slightly modified, but the inversion method would remain the same.

3.2 Generalization for n point sources

The objective of this part is to detail the inverse process used to robustly, automatically and rapidly estimate large quantities of data from the surface-measured IR films. Depending on the type of scanning, as illustrated in figure 3 and already modeled with respect to constant velocity in a previous paper [23], equation 1, available for only one point-like pulse thermal response, can be generalized as follows:

$$\theta_{\text{Scan}}(x,y,z,t) = \int_0^t \frac{Q\left(x',y',z'\right)}{\rho C_p} \frac{\exp\left(-\frac{(x-x')^2}{4a_x(t-\tau)}\right)}{\sqrt{4\pi a_x(t-\tau)}} \frac{\exp\left(-\frac{(y-y')^2}{4a_y(t-\tau)}\right)}{\sqrt{4\pi a_y(t-\tau)}} \frac{\exp\left(-\frac{(z-z')^2}{4a_z(t-\tau)}\right)}{\sqrt{4\pi a_z(t-\tau)}} d\tau \tag{5}$$

To obtain this model, the first assumption is to assume that the sum of equation 5 is obtained with complete relaxation or sufficient distance or repetitive time between the laser pulses to ensure that the baseline is null so that no influence from the neighboring source can occur. A detailed study of the scanning parameters and influences on the simplified proposed method that may occur if this assumption is not verified is discussed in the following section.

3.2.1 Influence of the scanning parameters

In this section, it is important to study the influences of pulse spatial and temporal distances. As already discussed in our previous paper [16], one way to overcome the source superposition problem is to apply the superposition principle by subtracting the first estimated source

from the set of measurements. Here, this approach requires knowledge of both space-time positions (x', y', τ) and trust in the position $e(z')$ estimated by the proposed method. In this study, considering the possibilities offered by laser scanning methods, it is proposed to study the alternatives to the superposition, especially the influence of the latter on the method of estimating the parameters of equation 4. The final objective is to provide a criterion guaranteeing good robustness. To this aim, and as shown in figure 4, the distance between two successive spots must be compared with the rise time of the temperature on the surface of the object and the τ (s) time between two impacts.

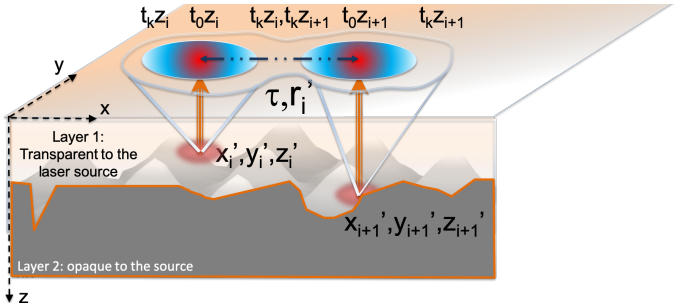

Fig. 4: Schema of the superposition principle with the important parameters

To begin, let us study the influence of a unique impact on the whole sample. The thermal response measured at the surface, given by equation 2, depends on the depth of the point source correlated with the thermal properties and, in particular, on the diffusion coefficient a_z of the studied layer. To take into account these two parameters, the Fourier number along the z direction, $Fo = a_z t/[e(z)]^2$, is introduced [17]. Then, for a given medium (with a given diffusivity), the deeper the source is, the smaller the Fo parameter is. In order to see the influence of this parameter on the thermal response at the surface, the results obtained for one pulse centered in an image are presented in figure 5 for four different values: $Fo = 0.01$, $Fo = 0.1$, $Fo = 1$ and $Fo = 10$. The data are presented along the x-direction for the line located at $y = 0$. In figure 5.a is represented the time corresponding to the maximum temperature measured at the given position and in figure 5.b the value of the maximum temperature. As the objective is to compare the thermograms, the data are normalized. T^* are the temperatures normalized by the maximum temperature value of all the thermograms, t^* are the times corresponding to the maximum of temperatures normalized by the maximum value of all the thermograms, and the space x^* is normalized by the total length (along the x-direction) on which the measurement is performed.

(a) **(b)**

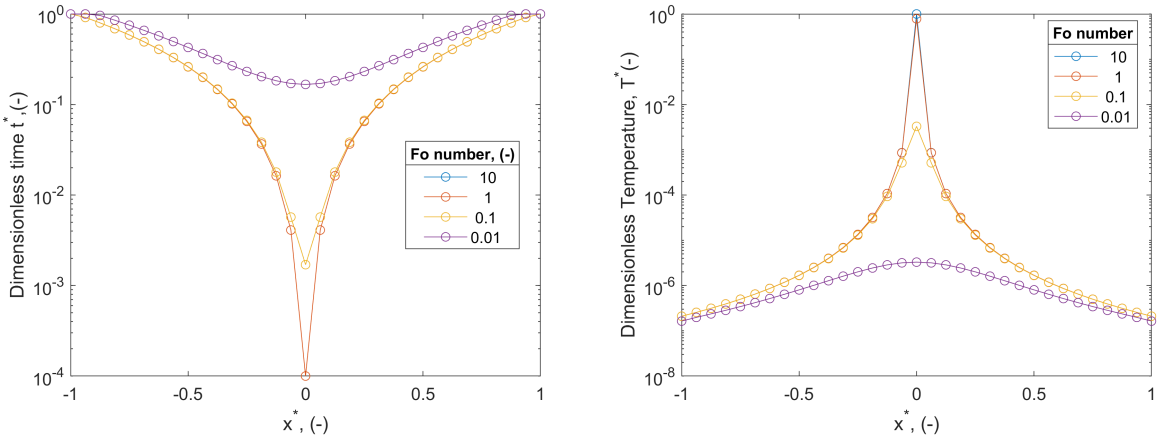

Fig. 5: Results obtained for one pulse centered in an image for four different Fourier number. The data are presented along the normalized x-direction for the line located at $y = 0$: a) normalized time corresponding to the maximum value of temperature b) value of the maximum temperature.

Thus, as seen in figure 5, if the point source is just below the surface (small thickness of layer 1), the maximum temperature measured at the surface at time t_{max} (time value corresponding to the maximum of temperature)) is high and is quickly reached, whereas if the point source is deep (small Fourier number), the temperature elevation at the surface is low and takes longer to be reached, and the influence on the neighboring pixels is high. Thus, the higher the Fourier number is, the greater the influence of a source on its neighbors.

Regardless of the depth of the source, the diffusion of the heat in the entire layer causes a temperature increase at the surface of the neighboring points, particularly for high Fourier numbers. Therefore, the study of the influences of the distance and time between several impacts must be conducted. Then, for a given sample (*i.e.*, a fixed Fourier number), three different cases can occur:

- $\tau < t_{max}$: "fast" scanning
- $\tau \approx t_{max}$: "moderate" scanning
- $\tau > t_{max}$: "slow" scanning

The example of 9 point sources located at the same depth (1 mm) in the layer and scanned in a square is studied here. Three constant scanning velocities are simulated, leading to three different time parameters τ between two impacts: $\tau = 0.1$ s, $\tau = 1$ s, and $\tau = 100$ s. In this example, $t_{max} = 1.9$ s and the thermal diffusivity was fixed at $a_z = a_y = a_x = 1.10^{-7}$ m^2.s^{-1}. The displacement of the laser is made from point 1 to point 9 in ascending order (figure 6.a) with a distance of 1.6 mm between two impacts. The dimensionless temperatures measured at the surface of each of the 9 points are illustrated in figures 6.b, 6.c and 6.d.

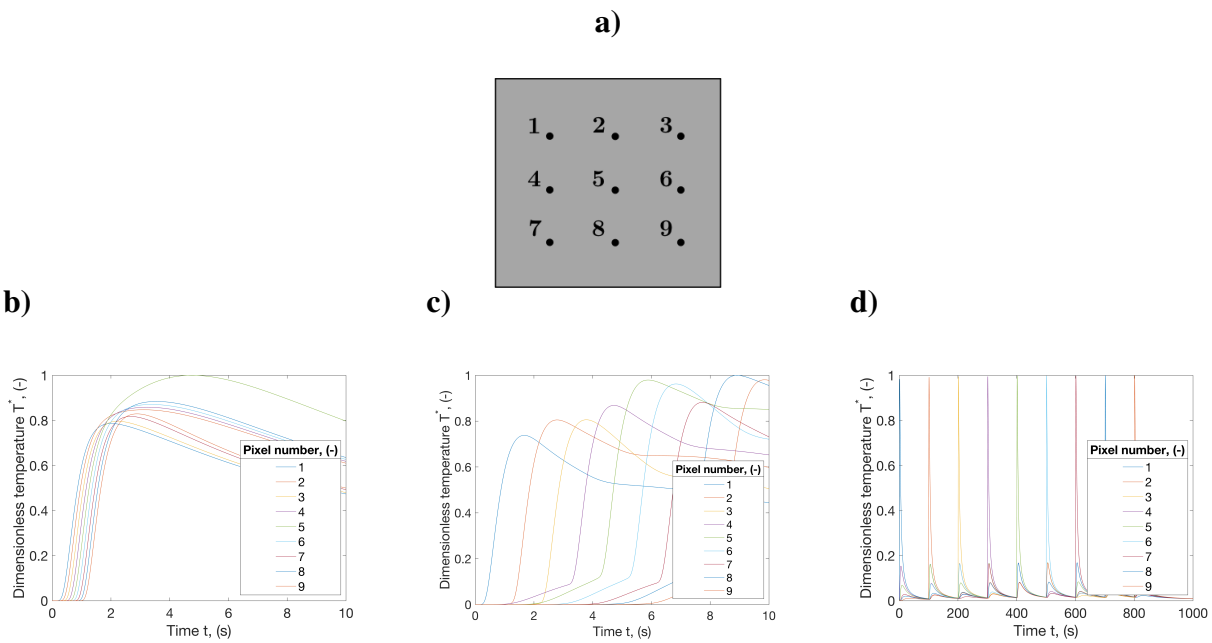

Fig. 6: Example of scanning parameter influences on the constant velocity flying spot technique. a) Schema of the 9 point sources located at the same depth in the layer. Dimensionless temperature T for different τ for the 9 pixels: b) τ = 0.1 s, c) τ = 1 s, d) τ = 100 s.*

For the three velocities used, the results enable the determination that the presence of several point sources influences the surface temperature. For "fast" scanning ($\tau = 0.1$ s), it is found that three groups can be differentiated at long times ($t > t_{max}$). The temperature of point 5, which has 8 neighboring sources, is higher than that of the points. The temperatures of the point sources 1, 3, 7 and 9, which have "only" three neighboring sources each, are the lowest, and the temperatures of the point sources 2, 4, 6 and 8, each with 5 neighbors, are in the middle. The differences within groups are due to the laser displacement direction. The same observations can be made for "slow" scanning ($\tau = 100$ s), but to a lesser extent. For "moderate" scanning ($\tau = 1$ s), the influences of neighboring sources are important at long times, but they are also present at very short times due to thermal diffusion phenomena.

Thus, a methodology is proposed in the following part in order to estimate the depth of each source despite the presence and influence of the neighboring sources.

3.2.2 Methodology for parameter estimation

The objective of this part is to detail the inverse process for n point sources. To do so, the main idea is to use the maximum sensitivity of the depth pulse response and to use the same reasoning as that of the back face flash (*cf.* work of Parker [22] and Degiovanni [24]). For each pixel (source), the measured temperature is then derived, and the point corresponding to the maximum of the derivative t_M is retained as the upper limit to estimate the slope of equation 4. Thus, the inverse process can be performed within the time interval $[t_0,\ t_M]$, where

t_0 is the time of the laser impact for the studied source. In the same way, to lessen the effect of neighboring sources at short times, the method can be performed within interval $[t_m,\ t_M]$, where t_m is adjusted to be within the optimal area of sensitivity to the slope of equation 4.

For each of the three cases presented in figure 6, parameters Y from equation 4 are plotted as functions of inverse of the time, as shown in figures 7.a, 7.b and 7.c.

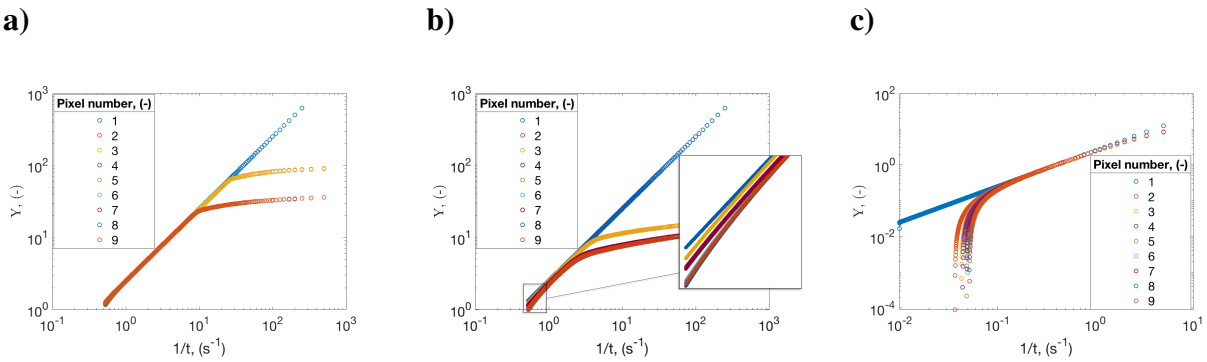

Fig. 7: Example of scanning parameter influences on the constant velocity flying spot technique. Representation of the expression of equation 4 for several τ values equal to: a) 0.1 s, b) 1 s and c) 100 s.

For all the time delays used ($\tau = 0.1, 1$ and 100 s), one can find a linear behavior of $Y(t)$. As discussed previously, linearity is not present at very short times (high values of $1/t$) or at long times (small values of $1/t$). Indeed, the influence of the neighboring pixels is strong both at short times (before the laser pulse) and at long times (heat rise of the neighboring pixels), particularly when $\tau = 1$ s.

In light of the above, for each measure, the calculation of the statistical correlation between the magnitude $Y(t)$ and $X(t)$ of equation 4 can be performed to optimize and determine the best values of t_m and t_M.

The focus on the case where the time between two laser pulses is small in front of the rise time, as illustrated by figure 6.a, is made here. The statistical correlation between the magnitude $Y(t)$ and $X(t)$ of equation 4 is calculated and represented in figure 8.b. The result obtained is shown in figure 8.a for the set of pixels of the example in figures 6.a). This study enables choosing the parameters t_m and t_M.

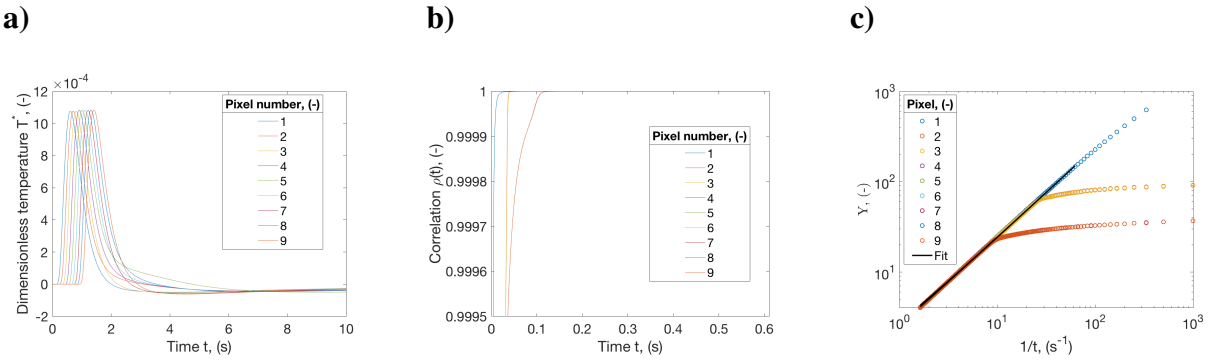

Fig. 8: Presentation of inverse processing principle: a) derivative of the temperature response illustrated in figure 6.a, b) calculated correlation from t_0 to the time corresponding to the maximum sensitivity and c) linear evolution of the temperature calculated with equation 4 and estimated slope in the range of correlation close to 1.

Pixel number	1	2	3	4	5	6	7	8	9
Theoretical Value	0.4								
Estimated Slope $\tau = 0.1$ (s)	0.3998	0.39952	0.3995	0.3994	0.3994	0.3994	0.3993	0.3994	0.3994
Error (%)	0.0599	0.1168	0.1170	0.1601	0.1580	0.1580	0.1635	0.1580	0.1580

Tab. 1: Estimated slope when applying the inverse processing and associated error.

In this case, the error of the estimated slope for each of the 9 pixels is very small (<0.2%).

3.3 Influence of Laser source absorption

The laser source is assumed to be collimated and totally absorbed at the interface. Nevertheless, the laser energy will be absorbed during its path through the studied layer according to the Beer-Lambert law:

$$Q(z) = I_0(1 - R)e^{-\beta z} \tag{6}$$

where I_0 (W) is the incident optical power of the laser, β (m^{-1}) is the absorption coefficient of the studied layer and R is the reflection coefficient.

The thermal response issued from equation 2 was calculated for the source as a function of z given by equation 6, as illustrated in figure 9.a. At short times, there is a significant difference between the theoretical model and the model with absorption. However, this difference quickly decreases and becomes negligible for long times. This result can be explained by the fact that at short times, the temperature due to shallow thermal sources is dominant over the temperature of the deepest (and most intense) sources. Indeed, although not very intense, these sources are close enough to the surface to manifest a significant temperature elevation. On the other hand,

at long times, sources close to the surface exert negligible action, and only the temperature due to the most intense source is significant.

(a) **(b)**

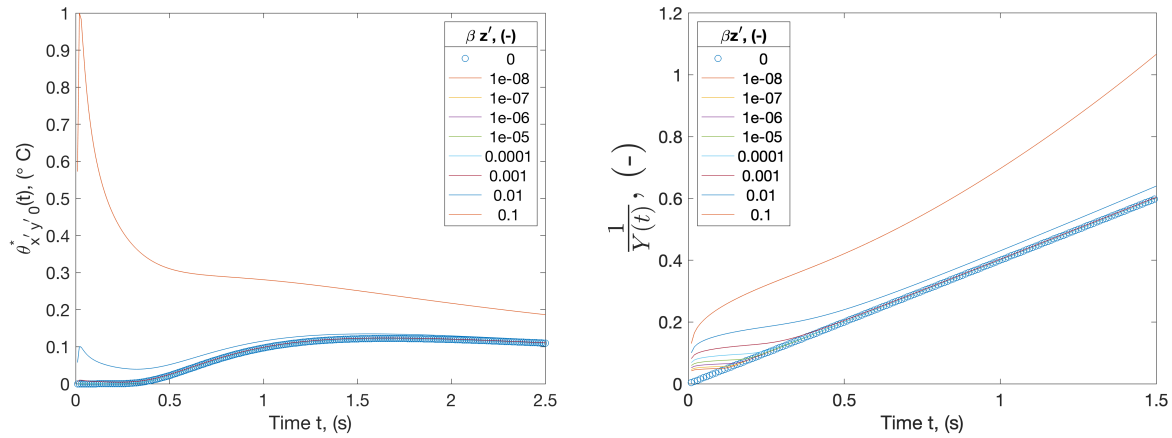

Fig. 9: a) Normalized front-face temperature as a function of several incident laser source absorptions in semitransparent resin and b) inverse of the $Y(t)$ expression of equation 4 as a function of time.

From the temperature in figure 9.a, the model of equation 4 can be calculated, as represented in figure 9.b, where we can clearly observe the effect of the absorption. In fact, for $\beta z < 0.01$, this influence occurs only at short times, and the linear behavior is reached after a few thousand ms. In contrast, for $\beta z \geq 0.1$, the linear behavior is never reached. The interesting point here is the limiting nature of this study. Indeed, the study shows that for layers with $\beta z < 0.01$, it will be possible to apply the contactless profilometry proposed here. Another interesting point is that with the advent of IR laser diodes [25], we can consider this approach in environments that are completely opaque to visible light. Thus, the multispectral nature of these sources can also allow controlled absorption in heterogeneous multilayer media.

4 Validation of the proposed method

4.1 Validation on a numerical case

To illustrate the thermal profilometry method, a bilayer of two homogeneous materials has been modeled. The lower layer is composed of a rough material (carbon epoxy), whereas the upper layer is composed of a resin that is applied on the material to obtain a smooth surface. In this example, the interface is modeled by a 2D-sinus function, which translates the roughness of the material by the formation of bumps and hollows. The amplitude variation of the sinus is chosen as 1 mm. The thickness average of the resin layer is 1 mm; it therefore varies between 0.5 and 1.5 mm due to the roughness of the lower layer. Here, the resin is

considered to be an isotropic material, with a diffusion coefficient given by $a = 1.10^{-7}$ m ^{2}.s $^{-1}$.

A laser will scan each pixel of this material (from bottom to top and from left to right) with a constant speed chosen such that $0 < \tau < t_{max}$. The studied surface is a square with dimensions 5 cm by 5 cm. The lower layer is considered opaque, and the upper layer is semitransparent to the wavelength of the laser. The energy deposited at the interface between the two layers is therefore considered constant, with a value set here as 7.5×10^{-8}J.m^2. An IR camera located above the sample will measure the resulting temperature at the surface of the material. The spatial periodicity of the heat source in this numerical example is 1.6 mm along each directions. The temperature data are computed in the first instance without the addition of noise. A study on the influence of the noise will be performed at the end of this section.

For each pixel of the surface, the proposed method, depicted in the previous sections, enables estimating the thickness of the material. Figure 10 illustrates the results obtained on the whole surface of the studied material. Figure 10.a illustrates the temperature measured at the surface during the process. The temperature evolution as a function of time is illustrated for five points on figure 10.b. Figure 10.c represents the maximum temperature amplitude for each pixel, and figure 10.d depicts its corresponding time. We can see that these data provide a first glimpse of the topography of the interface studied. Indeed, the highest temperature amplitudes correspond to small thicknesses, unlike "cold" points that correspond to greater thicknesses. We note that for the time of the maximum, the tendency is reversed: the temperature of the deepest points arrives later at the surface because of the greater distance to be covered. The gradient observed in figure 10.d is due to the laser scanning: the points furthest to the left are excited at short times by the laser, while those to the right are excited much later.

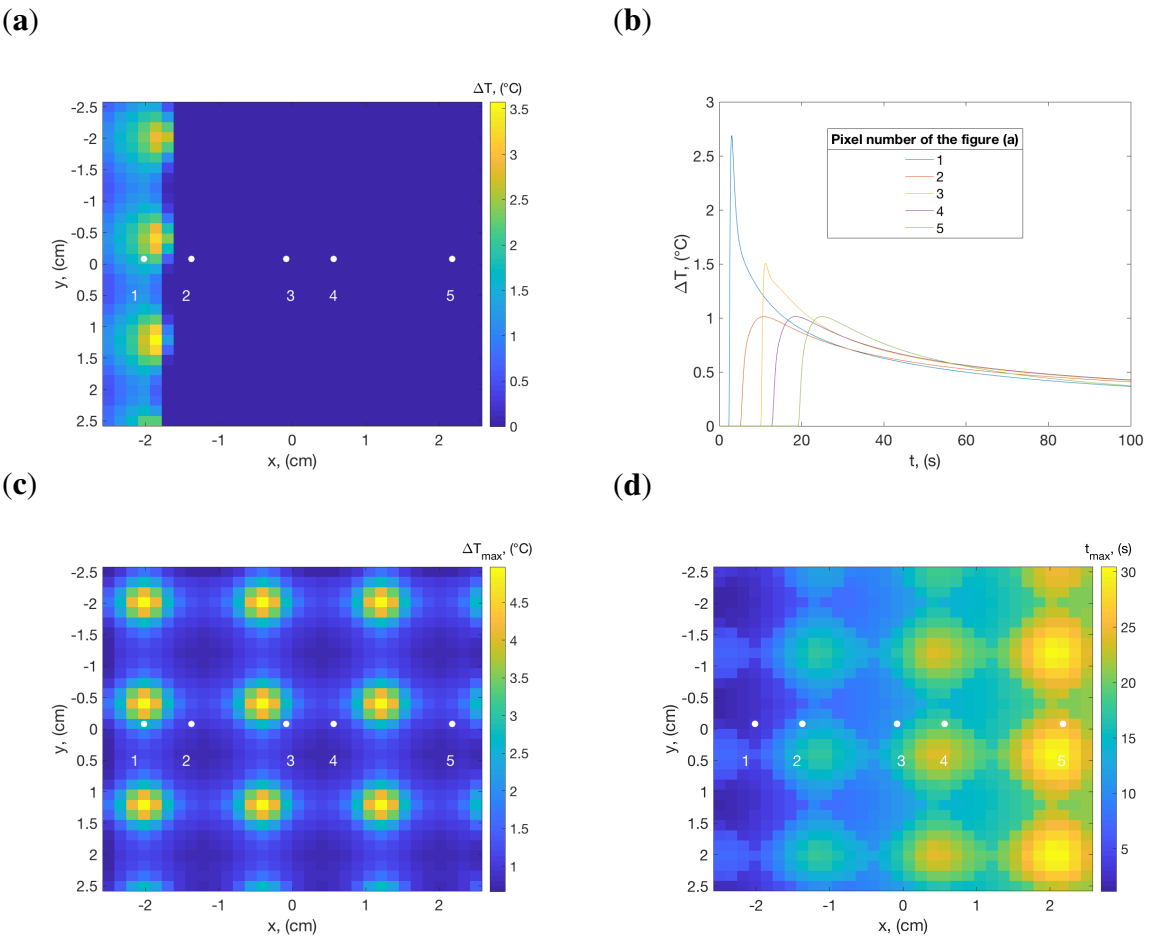

Fig. 10: a) Image of the temperature at the surface during the process, b) temperature as function of time for the five pixels highlighted on figure (a), c) maximum temperature values at each point of the surface and d) time corresponding with the maximum temperature value at each point of the surface.

The values of the thickness of the upper layer $e(z)$, or in other words the profile of the absorbent interface, are calculated with the proposed method, as illustrated in figure 11.a. The profile of the interface appears to be effectively reconstructed: the expected sinus-shaped roughness, with a resin thickness varying from 0.5 to 1.5 mm, is retrieved. To visualize the relevance of the results, the absolute error is calculated (in percentage) at each point, as illustrated in figure 11.b.

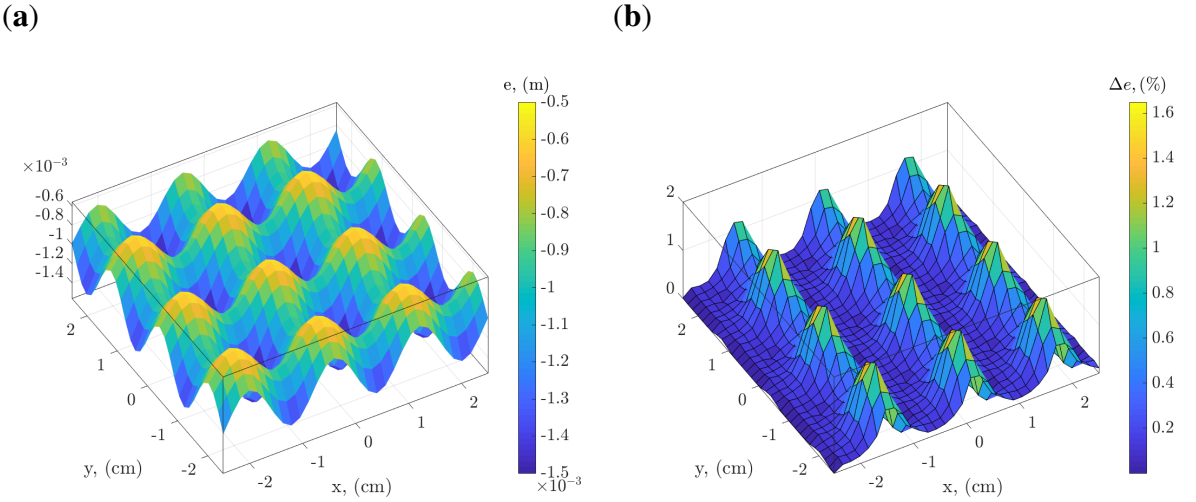

Fig. 11: a) Estimation of the first layer thickness (profile of the interface) and b) error between the theoretical and estimated thickness.

It can be seen that the highest errors are made for the deepest sources, however, they are minimal. This difference between theory and the estimation for the deepest source can be explained by the diffusive nature of the temperature and the influence of the neighboring sources closer to the surface. The temperatures of these sources reach the surface faster than those of the deepest sources, and with much greater intensity, and diffuse in all directions.

Study on the influence of the noise

The numerical example and the results illustrated by figure 11 were performed in an ideal case where the measured temperatures were noiseless. In this part, the influence of the noise on the method is studied. The focus is made on five contiguous excitation positions on the previous sample, corresponding to different thicknesses, as illustrated by figure 12.a. Three different noise levels are studied (SNR = Signal to Noise Ratio) and compared:

- SNR = $+\infty$: it corresponds to the previous case without noise.
- SNR = 200 : it corresponds to a moderate noise level.
- SNR = 20 : it corresponds to a high noise level.

The implemented noise in this part of study is a “white noise”, because it is the type of noise observed in thermal measurements. The SNR in thermal domain generally range between 10 to 100 000.

The five thermograms are illustrated in figure 12.b for SNR = $+\infty$, in figure 12.c for SNR = 200 and in figure 12.d for SNR = 20. For each of the five points, the time interval of study $[t_m, t_M]$, determined with the calculation of a statistical correlation as proposed in part 3.2.2,

is represented in figure 12.a with a black line. These time intervals of study are the same for each of the three noise levels. The methodology is then performed and the resulting data Y of equation 4 are plotted as function of $1/t$ for each noise level on figure 12.e, figure 12.f and figure 12.g respectively.

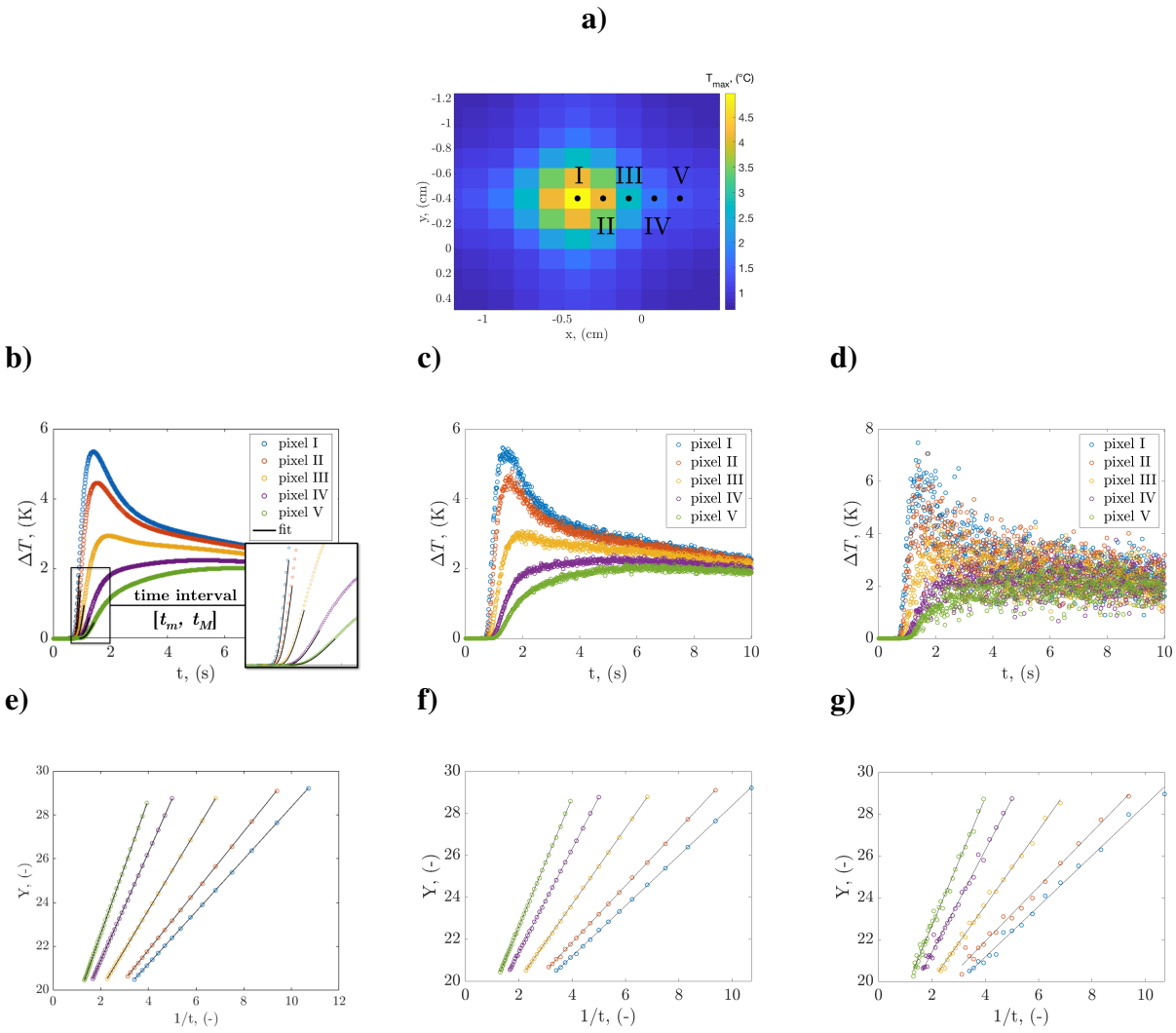

Fig. 12: Study on the influence of noise. a) Focus on five contiguous points corresponding to different thicknesses. Resulting temperatures at the surface for the five points for : b) no noise (SNR = $+\infty$), c) a moderate noise level (SNR = 200) and d) a high noise level (SNR = 20). Y as a function of $1/t$ on the time interval $[t_m, t_M]$ and their fit for each of the five points : e) for SNR = $+\infty$, f) for SNR = 200 and g) for SNR = 20.

For the five pixels, the same linear behaviour between Y and $1/t$ is retrieved, regardless of the noise level. The values of the corresponding thicknesses are then calculated and the absolute errors (in percentage) are given for each pixel in table 2. The errors are minimal (less than 2%), even in the worst case, with a very high noise level (SNR = 20).

Pixel number	I	II	III	IV	V
SNR = $+\infty$: Error (%)	0.01	0.02	0.02	0.01	0.04
SNR = 200 : Error (%)	0.01	0.04	0.08	0.11	0.11
SNR = 20 : Error (%)	0.7	0.49	0.03	1.29	1.20

Tab. 2: Relative error (in percentage) when applying the inverse processing for the 5 adjacent spots with the three different noise levels depicted by figure 12.

The low sensitivity to the noise is due to the choice of the time interval of study $[t_m, t_M]$. The estimation of the depth parameter is indeed always performed during the rise time of temperature. On this local area, the temperature variation is very high and therefore the sensitivity to noise is minimal.

For the setup presented in part 2 and through the use of the laser that can be very focalised, the noise level is very low and the SNR can easily go up to 1000. Thus, this example allows us to validate the proposed method and its ability to realize contactless thermal profilometry through a semitransparent layer added to an absorbent layer.

4.2 Application to Carbon-Resin composite materials

In this part, the results obtained on a carbon-resin composite pictured in figure 13 will be presented. Here, the studied composite exhibits groove-type defects in the resin-coated composite. The measurements were carried out on the rectangle delimited by the adhesive tape, which is located between typical defects. This defect was a groove in the composite media, perpendicular to the surface of the material. As the surface of the bilayer (composite + resin) is uniform, the thickness of the upper material (resin) is therefore greater at the location of the defect. After the estimation by the proposed thermal profilometer, a destructive testing was performed on the sample at the location of the defect : the resin layer has been scrapped of and the defect was measured with a mecanical comparator. The thickness of the resin was theoretically 300 μm. The objective here is to show that the thermal method proposed in this article allows us to detect and quantify the defect.

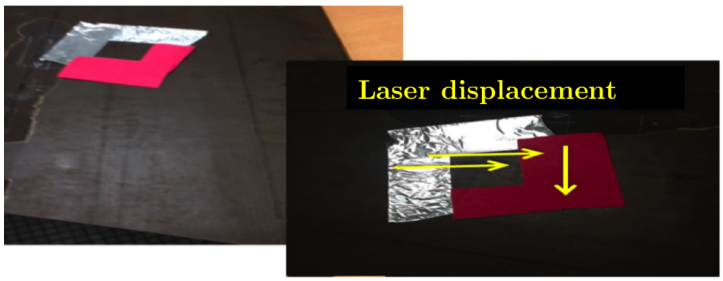

Fig. 13: Photography of the standard composite used in this study

To carry out these measurements, the laser diode presented in section 2 is used at full power with a very fast laser, with all pixels solicited. It should be recalled here that the experimental procedure undergoes a calibration phase that consists of converting the voltages (V) of the galvanometer mirrors into pixels. Then, the laser excitation is programmed in a loop on the number of pairs (*i.e.*, pixels). For each pair, the laser power is given, the pair of voltages for the mirrors is determined, and a pause time is employed, which allows for control of the time interval between two impacts. The resulting time τ between two laser impacts was then 9.1×10^{-4} s. The distance between two impact was 320 μm. The camera frequency rate was fixed to 500 Hz, and the final acquisition time was fixed at 30 s. The studied area forms a rectangle of dimensions 3.5 by 3.8 cm^2. The diffusion coefficient of the resin was measured by using the classical rear-face flash method [22] and was found to be 5.2×10^{-6} m^2.s^{-1}. To illustrate the measurements, the temperature fields as well as the thermogram of several pixels are represented in figure 14 for several time steps.

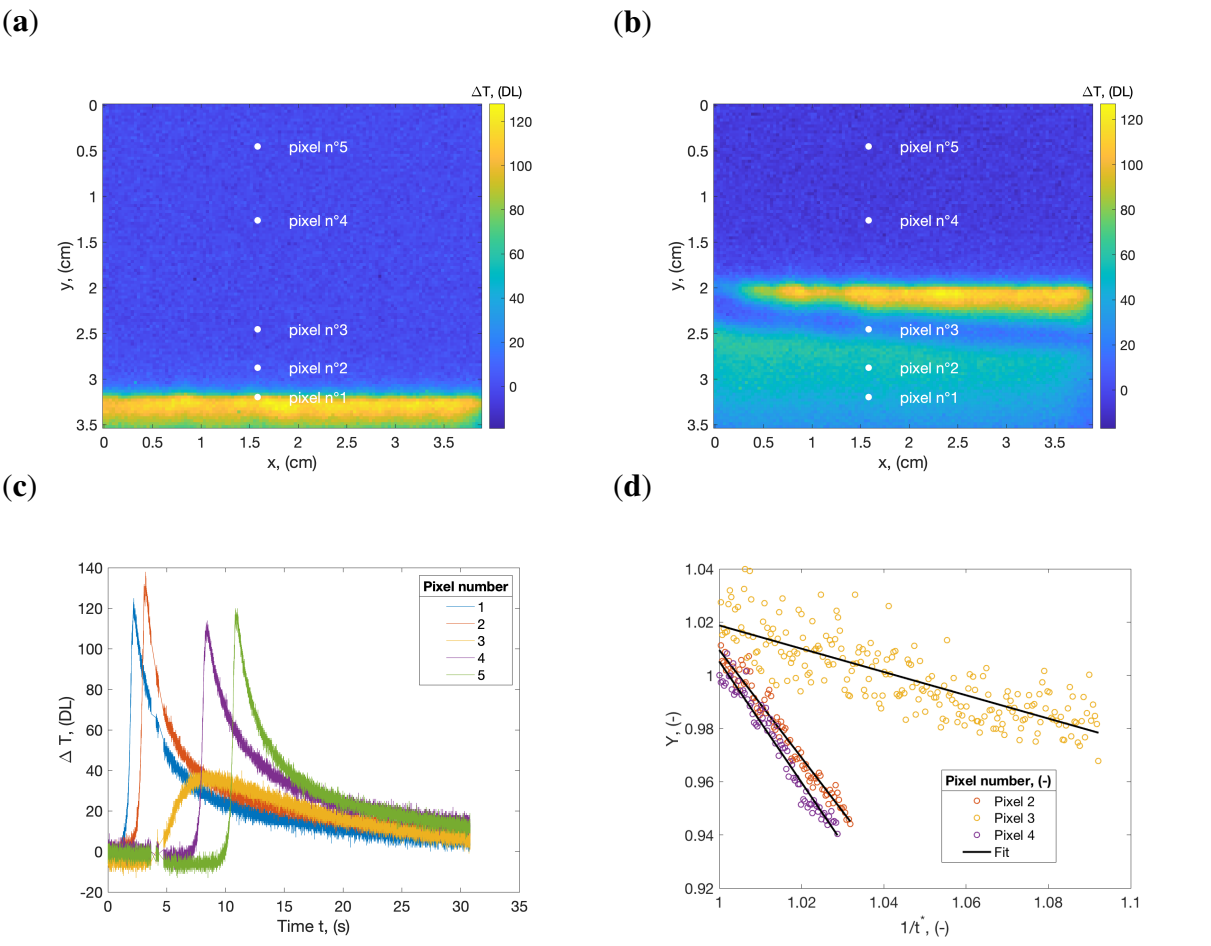

Fig. 14: Measured temperature fields as function of time: a) time step t = 2 s, b) time step t = 5.8 s. c) Extracted temperature as function of time for the pixels reported in figure 14.a. and d) Y as function of 1/t for the pixels 2, 3 and 4.

In the same way as for the synthetic case, the study of the maximum amplitudes and their corresponding times allows for a first glimpse of the studied profile. The two figures 14.a, 14.b enable observation of the laser displacement with increasing temperature. In particular, in figures 14.b and 14.c, the presence of a heterogeneity/crack in the carbon layer is indeed evident because it results in lower amplitudes of temperature and rising time.

Thus, at each point (pixel) of the surface, the thickness of the resin layer is calculated using the method proposed here, and illustrated in figure 14.d for the pixels 2, 3 and 4. Figure 15 shows the thickness (profile of fields) found at each point.

(a) **(b)**

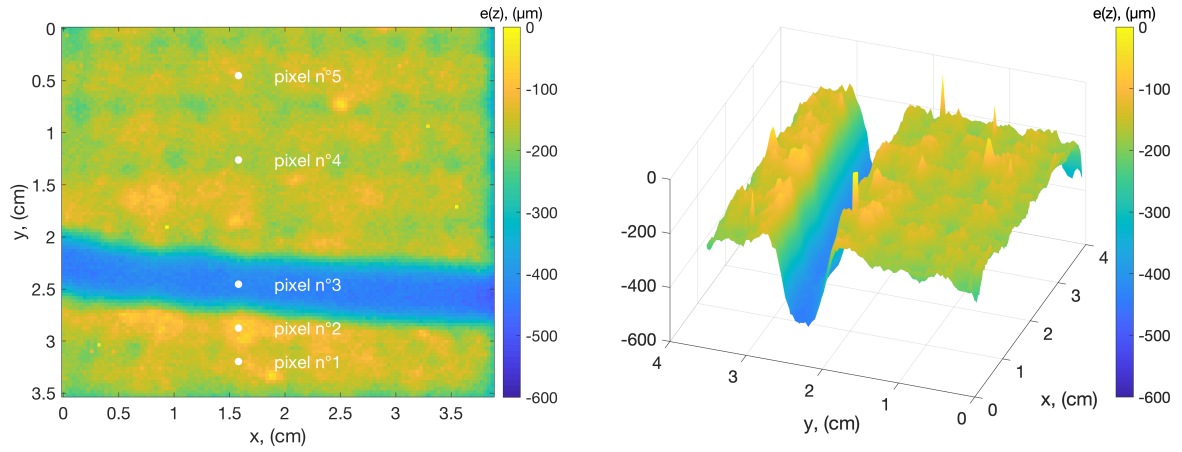

Fig. 15: Estimated fields of carbon profilometry (i.e., resin thickness): a) 2D mapping and b) 3D mapping.

The profile of the studied material is effectively retrieved in just a couple of minutes: the average thickness of the upper layer is 300 μm, except at the place of the crack, where the thickness is almost doubled. It can also be noted that the roughness of the carbon is retrieved, even where there is no defect.

The computer used is a laptop with 16 Go of RAM with a 3.1 GHz Intel Core i7 processor. However, any laptop is enough to execute this methodology because it does not require a special computing power.

In conclusion, the method of contactless thermal profilometry presented in this paper is fast and robust with respect to noise. This approach enables estimation of the profile of a material with accuracy.

5 Conclusion

In this paper, a method of contactless thermal profilometry is proposed. This approach enables estimation of the relief of different surfaces, which can be the interfaces between two media of a material. The proposed method is performed in real time, is very insensitive to noise and is therefore robust.

Acknowledgments

The authors acknowledge Epsilon Groupe Alcen for this study.

References

[1] Sayers, M. W. The little book of profiling: basic information about measuring and interpreting road profiles. Tech. Rep., University of Michigan, Ann Arbor, Transportation Research Institute (1998). 2

[2] Whitefield, R. Noncontact optical profilometer. *Applied optics* **14**, 2480–2485 (1975). 2

[3] Huang, D. *et al.* Optical coherence tomography. *science* **254**, 1178–1181 (1991). 2

[4] Fercher, A. F., Drexler, W., Hitzenberger, C. K. & Lasser, T. Optical coherence tomography-principles and applications. *Reports on progress in physics* **66**, 239 (2003). 2

[5] Wang, L. V. Ultrasound-mediated biophotonic imaging: a review of acousto-optical tomography and photo-acoustic tomography. *Disease markers* **19**, 123–138 (2004). 2

[6] Ntziachristos, V. & Razansky, D. Optical and opto-acoustic imaging. *Molecular Imaging in Oncology* 133–150 (2013). 2

[7] Ammari, H. *Mathematical Modeling in Biomedical Imaging II: Optical, Ultrasound, and Opto-Acoustic Tomographies*, vol. 2035 (Springer Science & Business Media, 2011). 2

[8] Ahmadi, S. Photothermal super resolution imaging: a comparison of different reconstruction techniques (2019). 2

[9] Burgholzer, P., Berer, T., Gruber, J. & Mayr, G. Super-resolution thermographic imaging using blind structured illumination. *Applied Physics Letters* **111**, 031908 (2017). 2

[10] Burgholzer, P. *et al.* Blind structured illumination as excitation for super-resolution photothermal radiometry. *Quantitative InfraRed Thermography Journal* 1–11 (2019). 2

[11] Waters, S., Burgholzer, P., Mendioroz, A. & de Ocáriz, I. S. 3d reconstruction of tilted cracks using infrared thermography and the virtual wave concept. In *Proceedings of the 14th International Conference on Quantitative Infrared Thermography, Berlin, Germany*, 25–29 (2018). 2

[12] Celorrio, R., Mendioroz, A. & Salazar, A. Characterization of vertical buried defects using lock-in vibrothermography: Ii. inverse problem. *Measurement Science and Technology* **24**, 065602 (2013). 2

[13] Mendioroz, A., Castelo, A., Celorrio, R. & Salazar, A. Defect characterization from lock-in vibrothermography data. *International Journal of Thermophysics* **36**, 1208–1216 (2015). 2

[14] Mendioroz, A., Castelo, A., Celorrio, R. & Salazar, A. Characterization and spatial resolution of cracks using lock-in vibrothermography. *NDT & E International* **66**, 8–15 (2014). 2

[15] Mendioroz, A., Celorrio, R., Cifuentes, A., Zatón, L. & Salazar, A. Sizing vertical cracks using burst vibrothermography. *NDT & E International* **84**, 36–46 (2016). 2

[16] Groz, M.-M., Abisset-Chavanne, E., Meziane, A., Sommier, A. & Pradère, C. Bayesian inference for 3d volumetric heat sources reconstruction from surfacic ir imaging. *Applied Sciences* **10**, 1607 (2020). 2, 6

[17] Groz, M.-M., Abisset-Chavanne, E., Meziane, A., Sommier, A. & Pradère, C. Three-dimensional reconstruction of thermal volumetric sources from surface temperature fields measured by infrared thermography. *Applied Sciences* **9**, 5464 (2019). 2, 5, 7

[18] Gaverina, L., Batsale, J., Sommier, A. & Pradere, C. Pulsed flying spot with the logarithmic parabolas method for the estimation of in-plane thermal diffusivity fields on heterogeneous and anisotropic materials. *Journal of Applied Physics* **121**, 115105 (2017). 2, 3, 6

[19] Beck, J. V., Cole, K. D., Haji-Sheikh, A. & Litkouhl, B. *Heat conduction using Green's function* (Taylor & Francis, 1992). 3

[20] Holland, S. D. Thermographic signal reconstruction for vibrothermography. *Infrared Physics & Technology* **54**, 503–511 (2011). 3

[21] Sommier, A. *et al.* Coupling pulsed flying spot technique with robot automation for industrial thermal characterization of complex shape composite materials. *NDT & E International* **102**, 175–179 (2019). 4

[22] Parker, W., Jenkins, R., Butler, C. & Abbott, G. Flash method of determining thermal diffusivity, heat capacity, and thermal conductivity. *Journal of Applied Physics* **32**, 1679–1684 (1961). 6, 9, 18

[23] Gaverina, L. *et al.* Constant velocity flying spot for the estimation of in-plane thermal diffusivity on anisotropic materials. *International Journal of Thermal Sciences* **145**, 106000 (2019). 6

[24] Degiovanni, A. Diffusivité et méthode flash. *Revue générale de thermique* **185**, 420–442 (1977). 9

[25] Humbert, G., Février, S., Druon, F. & Canning, J. Mid-infrared frequency conversion in highly nonlinear optical fibres. In *Proc. of SPIE Vol*, vol. 7714, 77140B–1. 12